Design, Fabrication, and Cold Test of a High Frequency System for an *H*-band Sheet Beam Travelling Wave Tube

Guoxiang Shu, Junzhe Deng, Lulu Xie, Guo Liu, Liang Zhang, Jianxun Wang, Zhengfang Qian, Wenlong He

***Abstract*- The design, fabrication and cold test of a high frequency system (HFS) for an *H*-band (220-325GHz) sheet beam travelling wave tube (SB-TWT) is presented in this paper. The HFS was composed of a 90-period double-staggered grating waveguide and a pair of identical L-shaped couplers with Bragg reflectors and matching steps. The HFS was manufactured by Nano-CNC machining and its electromagnetic properties were measured by using a vector network analyzer. The measured S-parameters were in good agreement with the simulated ones, which predicted a 3 dB bandwidth of ~47.0 GHz. The maximum value of the measured transmission coefficient S_{21} was -4.9 dB and the in-band port reflection S_{11} was around -15.0 dB. Based on the cold testing-based HFS, simulations of the beam wave interaction predicted a stable output power of over 55.1 W in the frequency range of 230-280 GHz. In addition, the instabilities of the beam wave interaction were investigated in the simulation.**

***Index Terms*—high frequency system, interaction instability, terahertz wave amplification, sheet beam travelling wave tubes.**

I. Introduction

The terahertz frequency band have received considerable interests due to their potential for diverse applications, including the high-resolution radars, high-data-rate wideband communications, electronic counter measures systems, and nonintrusive imaging [1]-[2]. So far, these applications have not been widely realized. One of the most significant factors is the lack of terahertz power amplifiers with moderate radiation power and wide bandwidth, thereby resulting in the expression "THz gap". The sheet beam travelling wave tube (SB-TWT) is a kind of competitive device that is helpful to fill the gap due to the high radiation power and broad bandwidth [3]-[6]. Compared with the pencil electron beam, the sheet electron beam (SEB) is advantageous as it could carry higher electron beam current by enlarging the lateral dimensions of the SEB [7]-[10]. As a result, the SEB with higher beam power contributes to higher power of SB-TWT. In addition, the planar configuration of the slow wave structure (SWS) associated with the SEB is relatively easier to machine.

In recent years, a variety of planar SWSs have been studied for millimeter-wave and terahertz SB-TWTs, including a 0.22 THz double-staggered grating waveguide (DSGW) [11], a *Ka*-band three-slot double-periodic staggered-ladder coupled-cavity [12], a *G*-band copper grating [13], a *V*-band microstrip meander [14], and a *W*-band sine waveguide [15]. Among these planar SWSs, the DSGW SWS has exhibited an intrinsically wide bandwidth and high power capacity. Likewise, different kinds of input/output couplers for SB-TWTs have been widely investigated, including an L-shaped power coupling structure with an oversized waveguide [16], a ridge loaded L-shaped waveguide with a cutoff waveguide [17], a L-shaped coupler with multistage matching steps and Bragg reflectors [18], a Y-shaped coupler and its improved versions [19]-[20], and a single branch waveguide coupler [21]. In this work, an *H*-band high frequency system (HFS) consisted of a DSGW SWS circuit and two L-shaped couplers with multistage matching steps and Bragg reflectors is studied.

When the operating frequency approaches to the terahertz band, the fabrication becomes increasingly challenging as the dimensions of the HFS scale with the operating wavelength. Furthermore the skin depth is in inverse proportion to the square root of the operating frequency, and the surface roughness has a significant effect on the ohmic loss and the transmission efficiency of the terahertz wave. More importantly, the assembling errors play a significant role in determining the electrical performance of the assembled micro-structures. A machining tolerance with a few microns, a surface roughness with hundreds of nanometers and a small assembling error are typically required in the fabrication of the HFS in a terahertz band SB-TWT. Considerable efforts have been made for the fabrication of the micro-structures in a terahertz vacuum electron device, such as the nano-computer numerical control (CNC) milling techniques [3], [15], [24]-[25], LIGA (German acronym for lithography, electroplating, and molding) process techniques [13], [26], deep-reactive ion etching (DRIE) techniques [26], wire cutting techniques [10], [27], and the 3D-printed mold electroforming [28].

Although in-depth studies of the couplers [18]-[21] and the DSGW SWS [6], [22]-[23] were conducted separately, this is our first report on the whole HFS. When the couplers and the SWS were combined together, the port reflection could be worsened and this could increase the risk of the oscillations. In this paper, matching steps were used to reduce the port reflections. The fabrication of the HFS also advanced the research of the SB-TWT at the terahertz frequency range. In

This work was supported by the National Natural Science Foundation of China (61901277), the Young Innovative Talents Foundation of Guangdong University (2018KQNCX215), the Science and Technology Foundation of Shenzhen (JCYJ20180305124406470), and the Natural Science Foundation of Shenzhen University (2018046).

G. X. Shu, J. Z. Deng, and W. He are with the College of Electronics and Information Engineering, Shenzhen University, Shenzhen 518060, China (e-mail: gxshu@szu.edu.cn; wenlong.he@szu.edu.cn).

L. L. Xie is with China Electronic Product Reliability and Environmental Testing Research Institute, Guangzhou 215011, China.

G. Liu and J. X. Wang are with the School of Electronic Science and Engineering, University of Electronic Science and Technology of China, Chengdu 610054, China.

L. Zhang is with the Department of Physics, SUPA, University of Strathclyde, Glasgow G40NG, United Kingdom.

Z. F. Qian is with the College of Physics and Photoelectric Engineering, Shenzhen University, Shenzhen 518060, China.

this work, an H-band (220-325GHz) HFS was machined by Nano-CNC machining and alignment islands and slots were introduced to reduce the alignment errors. It was shown that good machining and assembling accuracies were achieved. The cold test results were in good agreement with the simulation ones. Based on the cold testing-based model, the hot-cavity performances were studied. In addition, to study the interaction instabilities, PIC (particle-in-cell) models with different port reflections were simulated and zero-drive simulations were conducted.

The rest of the paper is organized as follows. The design and the characteristic analysis of the input/output coupler, the DSGW SWS, and the HFS are described in section II. Section III presents the machining and cold test of the optimized HFS. The beam wave interaction simulations and the analysis of interaction instabilities are presented in section IV. Finally, the paper is concluded in section V.

II. Analysis of Cold Cavity Characteristics

The HFS is one of the most critical parts of the SB-TWT. As shown in Fig. 1, it mainly consists of an input coupler, a DSGW SWS, and an output coupler. An input coupler is used to input the seed signal generated from a low-power terahertz signal source while allowing the SEB emitted from the electron-gun to propagate into the beam-wave interaction region. The modulated SEB would transfer its energy into the terahertz wave in the SWS circuit. The amplified terahertz wave would be coupled out through the output coupler. The spent electrons would propagate forward and finally be collected by a collector. Generally, a HFS with low reflection, high transmission, good isolation, wide bandwidth, and easy-to-machine configuration is desired.

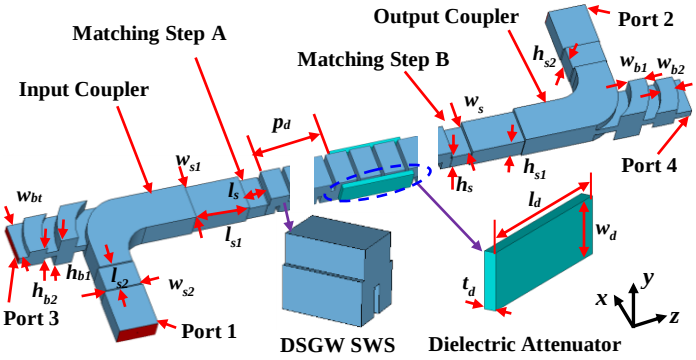

Fig. 1. A schematic diagram of the HFS composed by a DSGW SWS and two identical power couplers.

A、*Input/output couplers*

The L-shaped coupler with multistage matching steps and Bragg reflectors was used for the power coupling as it had good electrical performances and could be machined together with the DSGW SWS into two halves. The input and output couplers were identical in this work. As shown in Fig. 2, the L-shaped rectangular waveguide has a 90 °-bend, which allows the terahertz signal input to/output from the H-plane of the SWS. It contributes to the assembling of the magnetic focusing system typically placed over the E-plane of the DSGW SWS. Its corners were chamfered to reduce the reflection caused by the corner discontinuity. A rectangular SEB tunnel was embedded after the L-shaped rectangular waveguide, with a same height as the SEB tunnel in the DSGW SWS. To further compensate for the junction discontinuity and enhance the impedance matching, two matching steps were introduced. The L-shaped rectangular waveguide was connected with the SWS and the WR3-flanged rectangular waveguide through matching step 1 and 2, respectively. To enhance the isolation, two Bragg reflectors with low *Q*-factor were added over the SEB tunnel to reflect back the terahertz signal propagating towards port 3. A curved profile conformed to the L-bend in the wide side of the Bragg reflectors was adopted to ensure that the phase difference between these two structures was almost the same, which would be beneficial to achieve a better isolation between the port 1 and 3 in a wider frequency bandwidth.

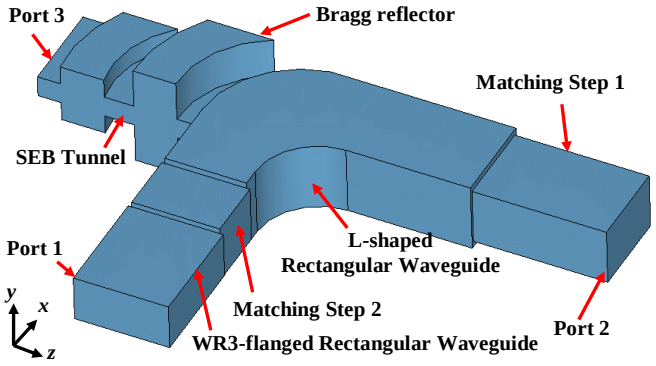

Fig. 2. A schematic diagram of the L-shaped rectangular waveguide with Bragg reflectors and matching steps.

In the simulation, the conductivity of the background material was set to be 2.0×10^7 S/m, which was the inferred value from the measured results presented in section III. The key dimensions of the input/output coupler were optimized by using CST Microwave Studio (CST-MWS) [29]. The optimized model with an electric-field (*E*-field) distribution at 250 GHz is shown in the inset of Fig. 3. An optimized bandwidth of ~58.3 GHz (222.1-280.4 GHz) with transmission coefficient S_{21} higher than -0.3 dB, port refection S_{11} and S_{22} smaller than -15.0 dB, and isolation coefficient S_{31} better than -28.0 dB was achieved. In additional to the excellent electrical performances, the fabrication of this coupler was relatively easy.

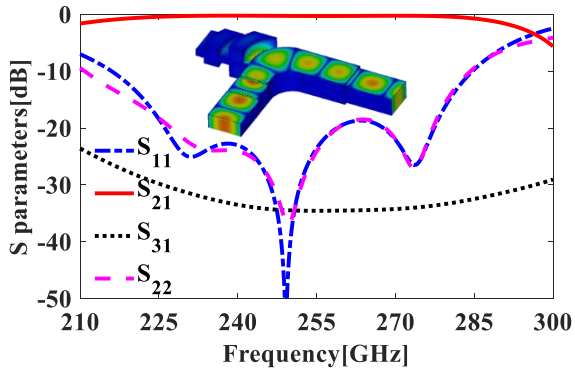

Fig. 3. Optimized S-parameters of the input/output coupler. The inset gives the optimized model with an *E*-field distribution at 250 GHz.

B、*DSGW SWS*

The dispersion property and coupling impedance were investigated by using an eigenmode solver in the CST-MWS. The inset of Fig. 4(b) shows the optimized model of a one-period DSGW SWS cell for dispersion analysis with a period L of 510 μm, width w of 690 μm, beam tunnel height h_{bt} of 120 μm, vane height h_v of 250 μm, and vane thickness t_v of 80 μm. As shown in the inset of Fig. 4(b), the DSGW SWS operated at the TM_{11}-like mode. It had a longitudinal component of the electric field (*E*-field), which was necessary for the longitudinal energy conversion between the terahertz wave and the SEB.

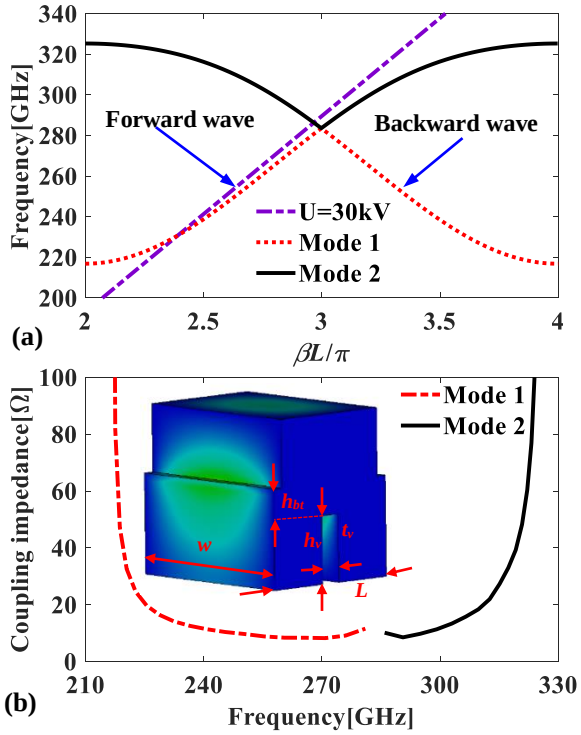

Fig. 4. (a) Dispersion curve and (b) average coupling impedance curve of the DSGW, β is the axial propagation constant. The inset shows the one-period DSGW SWS cell of the with an E-field distribution of mode 1.

Fig. 4(a) shows the dispersion curves of the DSGW SWS and the 30-kV beam line. A synchronism between the forward-wave and the 30-kV slow space charge wave in a wide bandwidth was achieved. The coupling impedance was used to represent the intensity of the beam wave interaction. The coupling impedance in Fig. 4(b) was the averaged value from 27 points uniformly distributed in the rectangular SEB tunnel, which was over 8.3 Ω throughout the frequency band.

C、*High Frequency System*

The HFS mainly consisted of a DSGW SWS circuit with 90 periods and two identical couplers as the input/output coupling structures. The attenuation to the electromagnetic wave by using the dielectric attenuators has been proved to be an effective method to suppress the interaction oscillations in the *Ku* and *Q* band SB-TWTs [6]. To suppress the potential oscillations, two identical dielectric attenuators made of BeO-SiC ceramic were loaded on the two H-planes of the SWS circuit, respectively. A lossy dielectric material with a permittivity of 12 and a loss tangent of 0.6 was used in the simulation. It should be noted that the made of the dielectric attenuators operating in the terahertz band is challenging. To minimize the reflections in the HFS, two identical matching steps A and B were introduced as shown in Fig. 1.

The effects on the reflection and transmission characteristics from some key parameters of the HFS were studied, including the electric conductivity σ of the background material, length of the dielectric attenuator l_d, width of matching step A(B) w_s, width w of the SWS. As shown in Fig. 5 (a), the transmission coefficient S_{21} would decrease when σ reduced due to the increase of the ohmic loss. As shown in Fig. 5 (b), S_{21} would suffer from a dramatic reduction when l_d increased, denoting a heavy attenuation from the dielectric attenuators. Such a heavy attenuation could also be achieved by increasing the width w_d and thickness t_d of the dielectric attenuator. Fig. 5 (a) and (b) showed that the ohmic loss and the attenuation from the dielectric attenuators were two key factors affecting the level of S_{21}. As shown in Fig. 5(c), w_s had a great effect on the port reflection S_{11}. When w_s was 0.7 mm, S_{11} was around -15 dB in a wide frequency bandwidth, denoting a good impedance matching. When w_s departed from 0.7 mm, S_{11} became worse. As depicted in Fig. 5(d), w had a great effect on S_{21}. The bandwidth of the passband would reduce with the decrease of w, which was caused by the increase of the cutoff frequency. The variation of some other parameters, such as l_{s2} and L, had slight effects on the S-parameters.

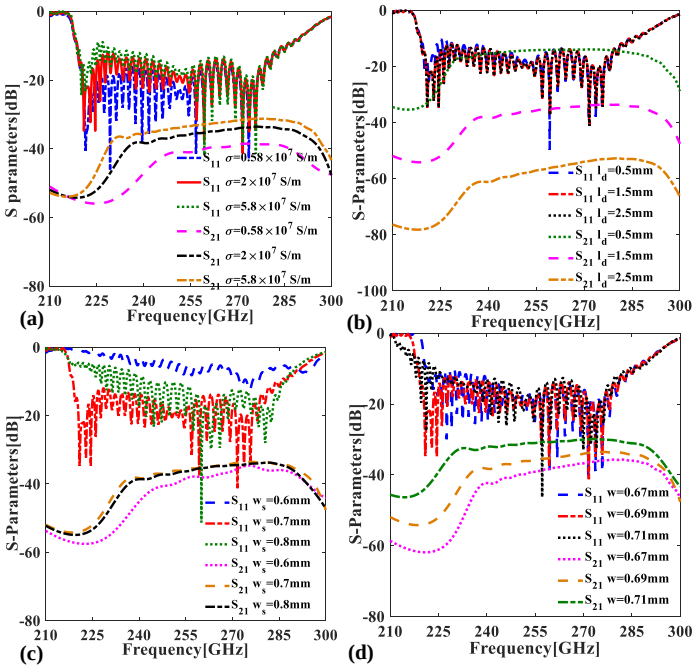

Fig. 5. Simulated port reflection S_{11} and transmission coefficient S_{21} at different values of (a) σ, (b) l_d, (c) w_s, (d) w.

In additional to the parameters mentioned above, the shape, position, and other dimensions of the dielectric attenuators as well as the dimensions of the matching steps were optimized by using the CST-MWS to achieve low port reflection and wide bandwidth of the pass band. The optimized values of the height h_s, length l_s, and w_s of matching steps A(B) were 0.41 mm, 0.60 mm and 0.71 mm, respectively. The optimized

values of the position p_d, t_d, w_d, and l_d of the dielectric attenuators were 17.5mm, 0.1 mm, 0.48 mm, and 1.5 mm, respectively. Fig. 6(a) and (b) show the optimized S-parameters of the HFSes without and with dielectric attenuators, respectively. Except for the dielectric attenuators, the other parameters of the two HFSes were kept the same. As shown in Fig. 6(a), S_{21} achieved a 3 dB bandwidth of ~62.5 GHz. S_{11} was smaller than -15.0 dB within a wide frequency bandwidth of ~ 60.0 GHz (219.5-279.5 GHz). The isolation coefficient S_{31} and S_{41} were both below -30.0 dB in a wide frequency bandwidth. As shown in Fig. 6(b), S_{21} decreased to < -34.0 dB in the whole frequency bandwidth after the introduction of dielectric attenuators. Although S_{11} was increased due to the introduced dielectric attenuators, the level of S_{11} was still in an acceptable range, which was around -15.0 dB in the frequency range of 219.3-281.0 GHz.

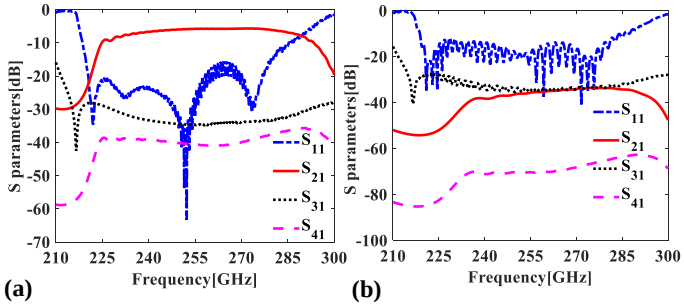

Fig. 6. Optimized S-parameters of the HFSes (a) without and (b) with dielectric attenuators.

III. Fabrication and Cold Test

To verify the designs, the optimized HFS was machined by using a CNC vertical machining center UVM-450C with a maximum rotation speed of 60,000 r/min. A machining accuracy of 2 μm and a surface roughness averages (R_a) of 40 nm was able to be achieved by using this machine. More importantly, to reduce the assembling errors, alignment island and slot were introduced. As shown in Fig. 7(a), the HFS was machined into two halves along the *E*-plane through the center of the beam tunnel. The maximum depth of the cut was up to 475 microns per half. One half of the HFS was machined at the center of an alignment island on an oxygen free high conductivity (OFHC) copper block. The other half was machined at the center of a matched alignment slot on another OFHC copper block. The island and slot were designed to precisely mate to each other with very tight tolerances in all dimensions. To further reduce the alignment errors, four pairs of small matching rectangular islands and recesses were machined at the four corners of the two halves.

The two machined halves were assembled together after the cleaning of each half. As shown in Fig. 7(b), a configuration with a size of 83 mm×16 mm×22 mm was achieved for the assembled device. A tight contact between the two halves was observed. The images of the DSGW SWS and the power coupler observed by an optical microscopy with an optical magnification of 20 are respectively shown in Fig. 8(a) and (b). The structural dimensions in the *xz* plane were measured. Table I makes comparisons between the designed and measured values of the dimensions. Most of the dimensions had a small deviation between the designed and measured values and the largest fabrication error was ~ 14 μm, showing a satisfactory machining.

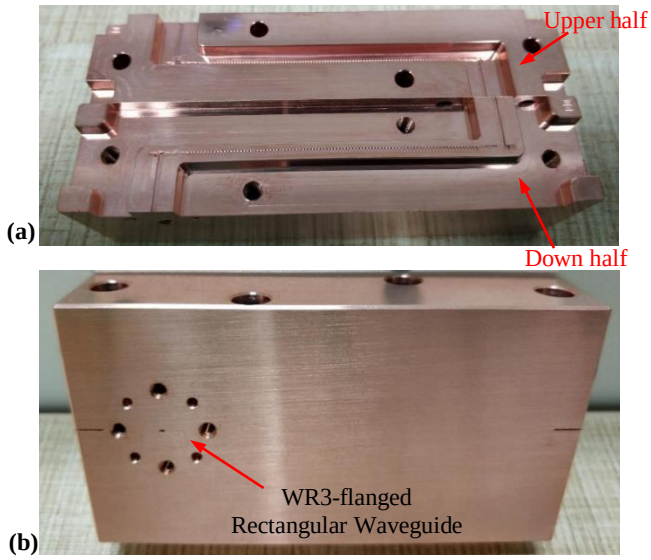

Fig. 7. Photo of (a) the upper and lower half of the manufactured HFS and (b) the assembled HFS.

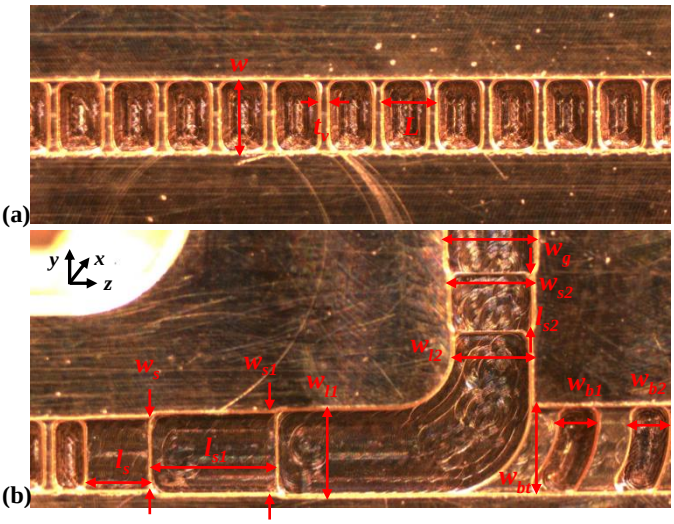

Fig. 8. Images of (a) the DSGW SWS and (b) power coupler observed by an optical microscopy.

The designed HFS in section II was remodeled to make the simulations to approach to the experimental measurements. The ohmic loss caused by the surface roughness was studied by using an effective conductivity [30]. In the remodeled HFS, the background material was set to be a lossy metal with a variable σ. Port 3 and port 4 were shorted due to the availability of a two-port vector network analyzer (VNA) and the lack of *H*-band matching loaders. Corner radius of 0.09 mm (tool diameter was 0.18 mm in this work) caused by the machining tool used in the nano-CNC milling was considered in the remodeled HFS. The alignment error between the two halves would probably happen in the process of assembly. In the remodeled HFS, a malposition of 0.06 mm along the *z*-axis was considered. In addition, all the designed dimensions in Table I were replaced by the measured ones in the remodeled HFS.

Table I Comparisons between the designed and measured dimensions.

Parameter	Description	Designed value [mm]	Measured value [mm]
w	Width of the SWS	0.690	0.680
t_v	Vane thickness in the SWS	0.080	0.081
L	Period of the SWS	0.510	0.507
l_s	Length of matching step A(B)	0.600	0.586
w_s	Width of matching step A(B)	0.710	0.708
l_{s1}	Length of matching step 1	1.200	1.187
w_{s1}	Width of matching step 1	0.780	0.787
l_{s2}	Length of matching step 2	0.550	0.536
w_{s2}	Width of matching step 2	0.800	0.801
w_{bt}	Width of SEB tunnel in the coupler	0.830	0.841
w_g	Width of the input waveguide	0.864	0.865
w_{l1}	Width 1 of the L-shaped waveguide	0.830	0.826
w_{l2}	Width 2 of the L-shaped waveguide	0.740	0.732
w_{b1}	Width of Bragg reflector 1	0.397	0.393
w_{b2}	Width of Bragg reflector 2	0.391	0.392

Fig. 9 presents the simulated S-parameters for the designed and remodeled HFSes, including the designed 4-ports HFS in section II using an σ of 2.0×10^7 S/m (HFS 1), the modified HFSes based on HFS 1 with an σ of 5.8×10^7 S/m (HFS 2), with an σ of 2.0×10^7 S/m and 2 ports (HFS 3), with an σ of 2.0×10^7 S/m, a chamfering r of 0.09 mm and 2 ports (HFS 4), with an σ of 2.0×10^7 S/m, a r of 0.09 mm, a modified w of 0.68 mm and 2 ports (HFS 5), and the final remodeled HFS based on HFS 5 considering the aforementioned malposition and fabrication errors (HFS 6). As shown in Fig. 9, some modifications brought great influences on the S-parameters, including the change of σ, the corner chamfering and the deviation of w. It showed that the aforementioned modifications, except for the σ, had small effects on the level of S_{21} in the passband. σ could be regarded as the crucial factor to decide the level of S_{21}. When σ was 2.0×10^7 S/m, the levels of the simulated and measured S_{21} agreed well. A surface roughness of ~150 nm was estimated when the effective conductivity was 2.0×10^7 S/m at 250 GHz [29], which was reasonable for the nano-CNC milling. The corner chamfering and the variation of w decreased the bandwidth of the passband around the lower frequency end and had a considerable effect on the port reflection S_{11}. In the simulation, a transmission dip occurred around 290.0 GHz when considering the malposition. Therefore, the measured transmission dip around 290.0 GHz was probably caused by the malposition in the process of assembly. Some other changes had tiny effects on the S-parameters, especially for the S_{21}, including the modification of the two isolation ports, small variation of most dimensions, such as t_v, l_{s2} and l_s.

Fig. 10 shows the assembled HFS without dielectric attenuators under cold test. The S-parameters were measured by using a well-calibrated VNA (AV3672E, 10 MHz-67 GHz) connected with two frequency extenders (AV3649A) with a frequency range of 220-325 GHz. As shown in Fig. 11, the measured S-parameters and the simulated ones of HFS 6 were in good agreement in a wide frequency band. As shown in Fig. 11, the measured S_{21} showed a pass-band with a 3 dB bandwidth of ~-47.0 GHz. The maximum measured value of S_{21} was -4.9 dB and the in-band port reflection S_{11} was around -15.0 dB. The measured results were indicative of satisfactory machining accuracy and surface roughness.

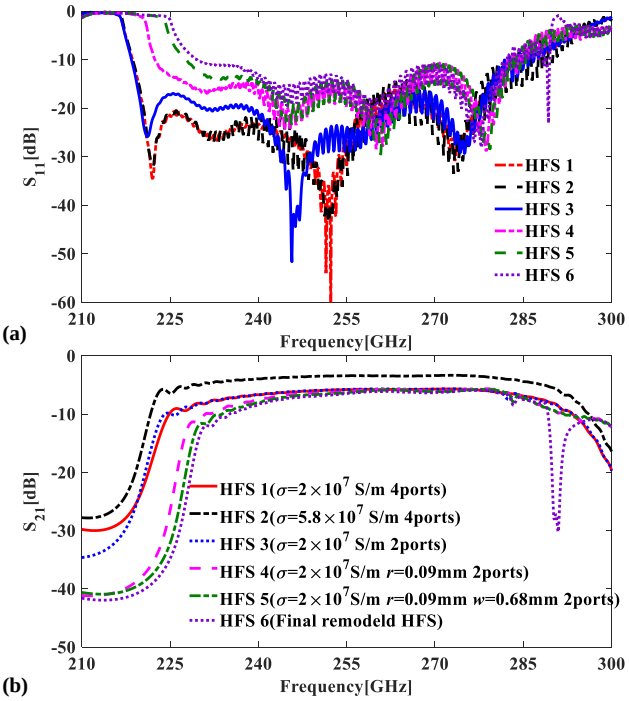

Fig. 9 Simulated S_{11} and S_{21} for different remodeled HFSes.

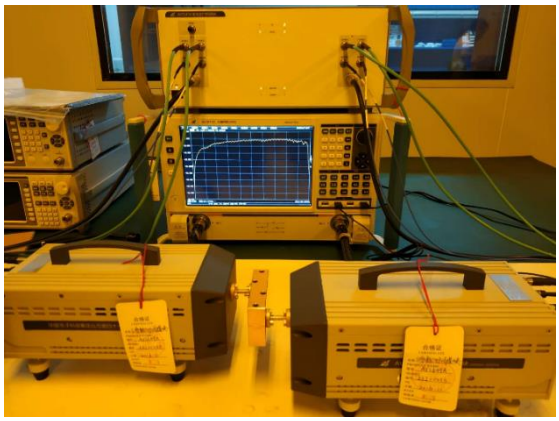

Fig. 10. VNA measurement setup of the assembled HFS.

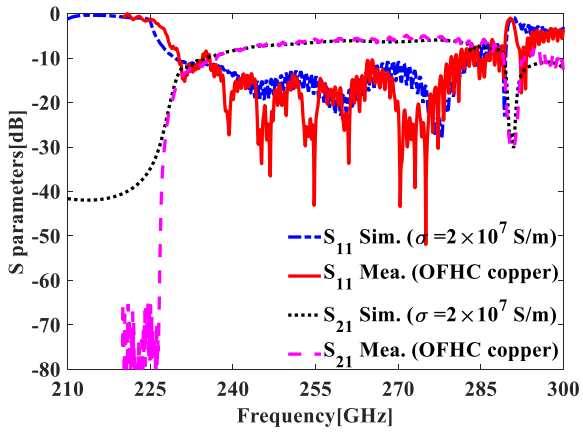

Fig. 11. Comparisons between the measured and simulated results.

IV. BEAM WAVE INTERACTION SIMULATIONS AND INSTABILITY ANALYSIS

A、Beam wave interaction simulations based on the cold testing-based model

To verify the designs and study the beam-wave interaction performances, PIC simulations were carried out by using CST Particle Studio. To make the simulations closer to the actual situation, the cold testing-based model in section III, i. e, the final remodeled HFS (HFS 6) was used. From the dispersion curve based on HFS 6, the optimal operating voltage has changed from 30 kV to 31.8 kV. A 31.8 kV, 0.2 A SEB with a transverse size of 0.6 mm×0.08 mm was injected into port 3 of the HFS with dielectric attenuators. The corresponding electron beam current density was ~416.7 A/cm^2, which could be provided by nanocomposite scandate tungsten cathodes [3]. The filling factor of the electron beam was 58.8%. A sine seed signal with a center frequency of 250 GHz and input power of 0.18 W was input from port 1. The amplified signal was observed at port 2 and the spent electrons were collected at port 4 by a metal short plane. To focus the SEB, a constant axial magnetic field of 1 T was used in the simulation.

The power flow was found to be maximized at the end of the DSGW SWS circuit and obvious beam electron bunching and energy conversion were also observed, implying effective beam-wave interaction. As shown in the inset of Fig. 12, a stable output voltage signal was observed at port 2. An output power of ~147.9 W was predicted with a corresponding gain of 29.1 dB and electronic efficiency of 2.3%. As shown in Fig. 12, the corresponding frequency spectrum obtained by fast Fourier transform (FFT) of the output signal was pure. The most prominent peak was at 250 GHz, which was the same as the frequency of the input signal.

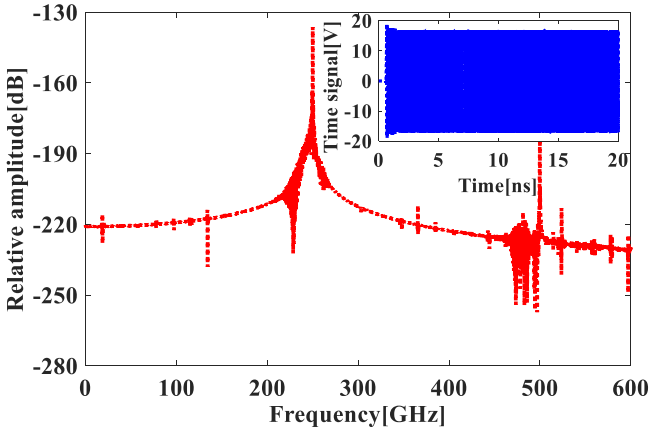

Fig. 12. Frequency spectrum obtained by FFT at 250 GHz. The inset gives the corresponding time-correlated output voltage of the amplified signal.

To estimate the in-band interaction performances of the SB-TWT, PIC simulations were conducted at some representative frequencies. Fig. 13 shows the performances when the beam wave interaction reached the saturated state, including the saturated output power P_{out}, gain, electronic efficiency, and the required input power to reach the saturated state P_{in}. The saturated P_{out}, gain, and the electronic efficiency were respectively higher than 55.1 W, 16.8 dB, and 0.87% in the frequency range of 230-280 GHz (50 GHz). PIC simulations with an equal input power of 0.18 W were also conducted at these representative frequencies. As shown in Fig. 13(a), the output power and gain were respectively higher than 2.9 W and 12.0 dB within the frequency bandwidth. The reduction of the power and gain at these representative frequencies was due to the fact that the interactions were under the unsaturation state.

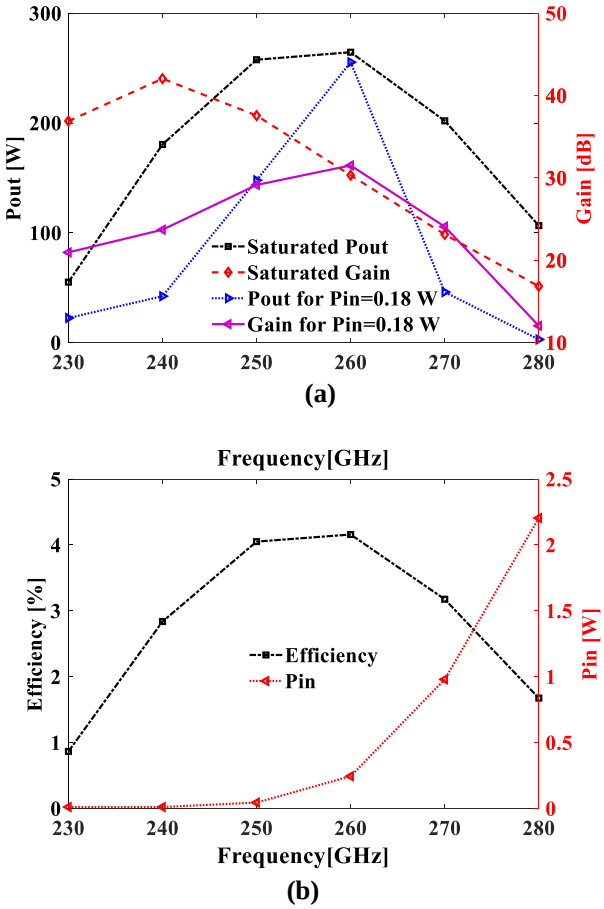

Fig. 13. (a) In-band P_{out} and Gain for the saturated state and an equal input power of 0.18 W. (b) In-band electronic efficiency and the required input power to reach the saturated state P_{in}.

The sensitivity of the beam wave interaction performance to the variation of the HFS's dimensions was carried out. From the PIC simulations at 250 GHz with an input power of 0.18 W, it was found that the interaction performance was not sensitive to the variation of some structural dimensions, such as the height of matching step 2 h_{s2} and t_v, as shown in Fig. 14(a) and (b). However, the variation of a small part of dimensions had non-negligible effects on the output characteristics of the SB-TWT, such as L. Fig. 14(c) gives the interaction performance dependent on L while keeping any other parameters unchanged. It was shown that when L was deviated to 0.49 mm and 0.53 mm, the amplifier would fail to work at the upper (such as at 240-280 GHz) and lower (such as at 230 GHz) band, respectively. It was due to that the deviation of L would directly affect the synchronous condition. When L was changed, the dispersion curves of the SWS mode and beam mode would both change and the operating voltage needed to be adjusted to re-reach the synchronous condition.

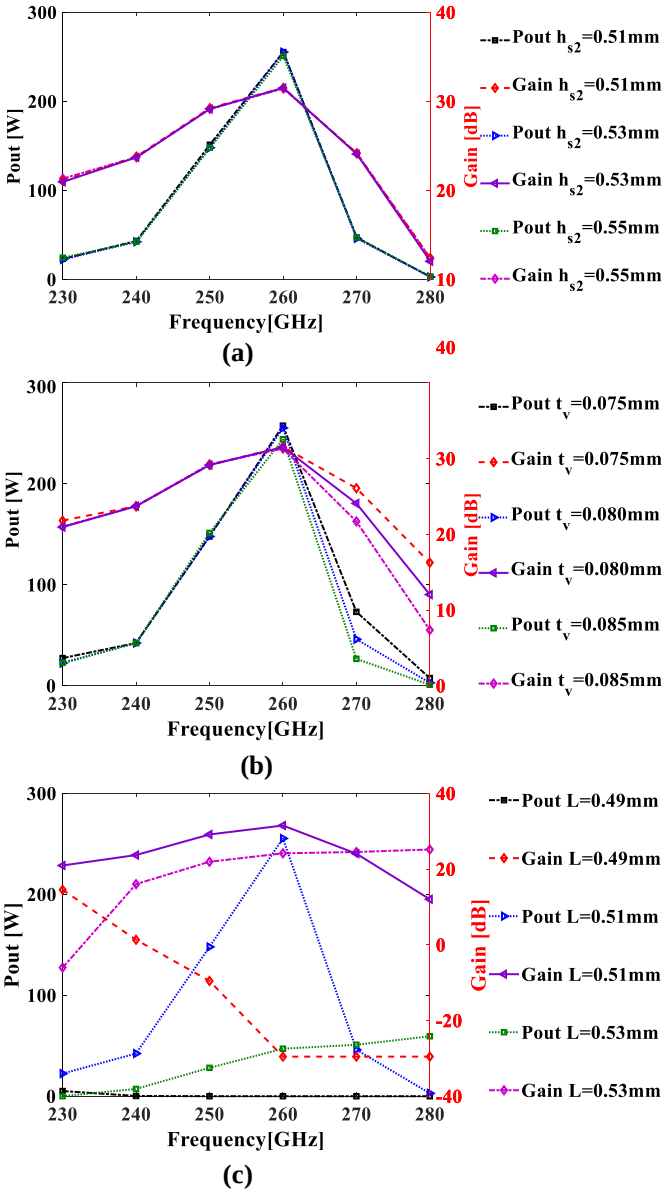

Fig. 14. Beam wave interaction performance at 250 GHz dependent on the variation of some structural dimensions, including (a) h_{s2}, (b) t_v, (c) L.

B、Investigation of the interaction instability

In a TWT, the interaction instability was easily caused by three types of oscillations: (a) regenerative oscillation, which was generally caused by the partial reflections at the input, sever, and/or output ends of the amplifier, (b) backward wave oscillation, and (c) absolute instability near the band edges [31]. When the SWS and couplers were combined, the port reflection would probably increase. More importantly, the fabrication and assembly errors tended to cause a high reflection in the actual situation. The instability analysis was conducted from two aspects: (a) PIC simulations based on HFS 6 under different port reflections and (b) zero-drive simulations based on HFS 6 under different beam voltages.

To study the effects of the port reflection on the stability of the beam wave interaction, S_{11} was intentionally worsened. The change of S_{11} was realized just by adjusting the height h_s and width w_s of matching step A(B) and keeping any other parameters unchanged. Such a change would not affect the beam wave interaction region. The simulations of the beam wave interaction under different S_{11} were conducted while all the other operating parameters were fixed, for example, the frequency and power of the seed signal were fixed at 250 GHz and 0.18 W, respectively. Table II gives the performances of the tube under some representative S_{11}. It was found that a stable output could be achieved even though the port reflection reduced to a low level, for example -3.4 dB. As shown in the inset of Fig. 15, a ripple was firstly observed in the output signal, but finally the output signal became stable. In addition, the corresponding frequency spectrum was clean. The stable operation under such a low S_{11} was probably attributed to the heavy attenuation from the dielectric attenuators. Generally, the regenerative oscillation would occur if the following equation was satisfied [32].

$$G > L + \tau_{in} + \tau_{\text{out}} \tag{1}$$

where G is the gain of the TWT, L is the circuit loss, τ_{in} and τ_{out} are the reflection coefficients at the input and output ports, respectively. All the parameters are expressed in decibels and positive values. Due to the heavy attenuations, for example 38.5 dB as shown in Table II, the value of the right-hand side of Eq. (1) was still high (~45.3 dB) enough to prevent the regenerative oscillation happening. As shown in Table II, the P_{out}, gain, and efficiency were decreased with an increase of S_{11}. This was probably due to that the input power taking part in the beam wave interaction would decrease with an increase of S_{11}, resulting in an unsaturated operation condition.

To study the band edge oscillations, zero-drive simulations under different beam voltages were conducted. As shown in Fig. 16(a), a time-domain output signal with a large magnitude of ~10.4 V was observed when the beam voltage was 31.5 kV. As shown in Fig. 16(b), an obvious peak with a large relative amplitude at 290.9 GHz was observed in the corresponding frequency spectrum. Although a few peaks were also found at the lower frequency band edge, for instance 214.4 GHz and 233.4 GHz. However, their relative amplitude were much smaller than the one around the upper frequency band edge (The relative amplitude at 290.9 GHz and 233.4 GHz were -144.5 dB and -233.4 dB, respectively). Hence, the upper band edge oscillation dominated in this zero-drive simulation. Such a simulation result agreed with a conclusion given in reference [31] "An absolute instability will occur if the dispersion diagram is convex at that point if the beam line intersects the backward wave side of the circuit dispersion curve".

TABLE II

Simulated interaction performances for HFS 6 with different port reflections S_{11} at 250 GHz. (*Eff.* represents the electronic efficiency)

w_s [mm]	h_s [mm]	S_{11} [dB]	S_{21} [dB]	P_{out} [W]	Gain [dB]	*Eff.* [%]	Oscillation
0.62	0.81	-3.4	-38.5	117.0	28.1	1.84	No
0.62	0.61	-4.8	-36.8	128.0	28.5	2.01	No
0.62	0.41	-8.0	-35.0	134.5	28.7	2.11	No
0.65	0.41	-11.3	-34.5	141.1	28.9	2.22	No
0.68	0.41	-12.0	-34.3	147.9	29.2	2.33	No
0.71	0.41	-14.5	-34.1	147.9	29.2	2.33	No

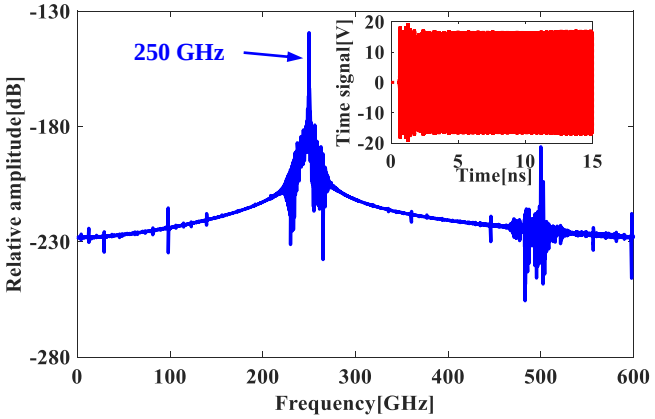

Fig. 15. Frequency spectrum obtained by FFT at 250 GHz (S_{11} was -3.4 dB). The inset gives the corresponding time-correlated output voltage of the amplified signal.

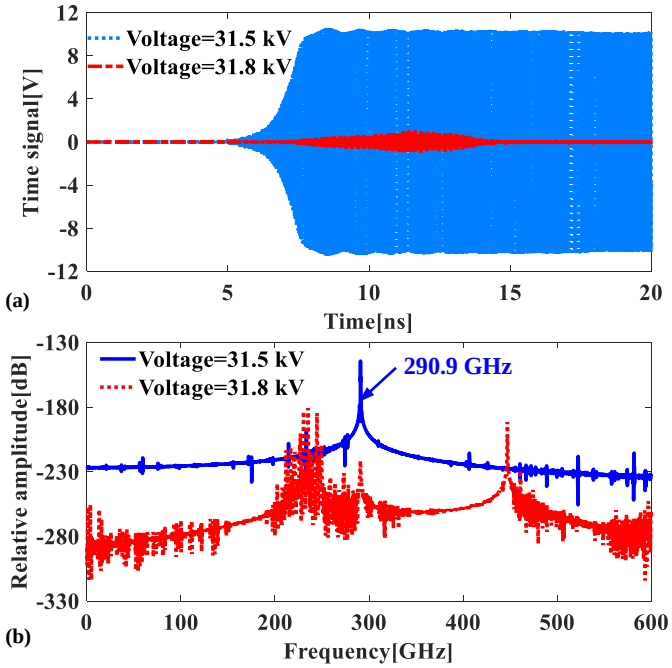

Fig. 16. Zero-drive simulation results under the beam voltage of 31.5 kV and 31.8 kV. (a) Time-domain output signal. (b) Frequency spectrum obtained by the FFT.

As shown in Fig. 16(a), the magnitude of the output signal greatly reduced and finally approached to zero when the beam voltage increased to 31.8 kV. As shown in Fig. 16(b), a peak around 290.9 GHz also appeared in the frequency spectrum. However, its relative amplitude was much smaller than the one in the above 31.5 kV-model. Some peaks were also observed at the lower frequency band edge. Their relative amplitude was larger than the one observed around 290.9 GHz. Hence, the lower band edge oscillation dominated in this model. The magnitude of the output signal (See Fig. 16(a)) and the maximum relative amplitude of the peaks (See Fig. 16(b)) observed in the 31.8 kV-model were both much smaller than the corresponding ones in 31.5 kV-model. Therefore, it would be much easier to suppress the potential band edge oscillations when the beam voltage was 31.8 kV. Choosing an appropriate beam voltage would be helpful to suppress the band edge oscillations.

In spite of the aforementioned band edge oscillations, stable beam wave interactions still could be obtained. As shown in Fig. 12 and 15, stable output signals and clean frequency spectrums were obtained when the beam voltage was 31.8 kV. Input-drive simulations under 31.5 kV were also carried out. It was found that stable outputs were also achieved in a wide frequency band centered at 250 GHz. It was showed that the band edge oscillations could be suppressed if the interaction between the SEB and the input signal was intensive enough.

V. Conclusion

An *H*-band HFS comprised of a 90-period DSGW and two identical *L*-shaped coupler with Bragg reflectors and matching steps as the input/output couplers was designed and studied. We have demonstrated a successful cold test on the nano-CNC milled HFS. Measured S-parameters matched well with the simulated ones, which predicted a 3 dB bandwidth of ~47.0 GHz. The maximum transmission coefficient S_{21} of -4.9 dB and port reflection S_{11} of around -15.0 dB were measured over that frequency bandwidth. Based on the cold testing-based HFS, the performances of the beam wave interaction, including the amplification characteristics and the interaction instabilities, were studied. It showed that a stable output power higher than 55.1 W was achieved in a wide bandwidth of 50 GHz (230-280 GHz). The designed HFS is adequate to be used in the construction of an SB-TWT operating at the *H*-band.

Reference

[1] J. H. Booske, R. J. Dobbs, C. D. Joye, C. L. Kory, G. R. Neil, G. S. Park, J. Park, and R. J. Temkin, "Vacuum electronic high power terahertz sources," *IEEE Trans. Terahertz Sci. Technol.*, vol. 1, no. 1, pp. 54-75, Sep. 2011, doi: 10.1109/TTHZ.2011.2151610.

[2] S. S. Dhillon, M. S. Vitiello, E. H. Linfeld, et al, "The 2017 terahertz science and technology roadmap," *J. Phys. D: Appl. Phys.* vol. 50, no. 4, pp. 043001-043049, 2017, doi:10.1088/1361-6463/50/4/043001.

[3] A. Baig, D. Gamzina, T. Kimura, J. Atkinson, C. Domier, B. Popovic, L. Himes, R. Barchfeld, M. Field, and N. C. Luhmann, Jr. , "Performance of a nano-CNC machined 220-GHz traveling wave tube amplifier," *IEEE Trans. Electron Devices*, vol. 64, no. 5, pp. 590-592, Aug. 2017, doi: 10.1109/TED.2017.2682159.

[4] D. E. Pershing et al., "Demonstration of a wideband 10-kW Ka-band sheet beam TWT amplifier," *IEEE Trans. Electron Devices*, vol. 61, no. 6, pp. 1637–1642, Jun. 2014, doi: 10.1109/TED.2014.2304473.

[5] P. D. Gensheimer, C. K. Walker, R. W. Ziolkowski, and C. D. Aubigny, "Full-scale three-dimensional electromagnetic simulations of a terahertz folded-waveguide traveling-wave tube using ICEPIC," *IEEE Trans. Terahertz Sci. Technol.*, vol. 2, no. 2, pp. 222-230, Mar. 2012, doi: 10.1109/TTHZ. 2011. 2178931.

[6] J. Wang, G. Liu, G. X. Shu, Y. Zheng, Y. Yao, and Y. Luo, "The PCM focused millimeter-wave sheet beam TWT," *in Proc. 18th Int. Conf. Vac. Electron. (IVEC)*, London, U.K., Apr. 2017, pp. 1-2, doi: 10.1109/IVEC.2017.8289528.

[7] J. Zhao et al., "Scandate dispenser cathode fabrication for a high-aspect-ratio high-current-density sheet beam electron gun," *IEEE Trans. Electron Devices*, vol. 59, no. 6, pp. 1792–1798, Jun. 2012, doi: 10.1109/TED.2011.2109723.

[8] J. X. Wang, L. R. Barnett, N. C. Luhmann, Jr., Y.-M. Shin, and S. Humphries, "Electron beam transport analysis of W-band sheet beam klystron," *Phys. Plasmas*, vol. 17, no. 4, pp. 043111-1-043111-11, 2010, doi: 10.1063/1.3383053

[9] W. Jiang, J. Wang, Y. Luo, L. Xu, X. Yao, and S. Wang, "Thermal analysis of sheet beam gun for the sheet beam traveling wave tube," *IEEE Trans. Electron Devices*, vol. 63, no. 3, pp. 1312-1316, Mar. 2016, doi: 10.1109/TED.2016.2519041.

[10] G. X. Shu, L. Zhang, H. Yin, J. Zhao, A. D. R. Phelps, A. W. Cross, G. Liu, Y. Luo, Z. F. Qian, and W. He, "Experimental demonstration of a terahertz extended interaction oscillator driven by a pseudospark-sourced

sheet electron beam," *Appl. Phys. Lett.*, vol. 112, no. 4, pp. 033504-1-033504-4, Jan. 2018, doi:10.1063/1.5011102.
[11] Y. M. Shin, L. R. Barnett, and N. C. Luhmann, Jr., "Phase-shifted traveling-wave-tube circuit for ultrawideband high-power sub-millimeter wave generation," *IEEE Trans. Electron Devices*, vol. 56, no. 5, pp. 706-712, May 2009, doi: 10.1109/TED.2009.2015404.
[12] P. B. Larsen, D. K. Abe, S. J. Cooke, B. Levush, T. M. Antonsen, and R. E. Myers, "Characterization of a Ka-band sheet-beam coupled cavity slow-wave structure," *IEEE Trans. Plasma Sci.*, vol. 38, no. 6, pp. 1244-1254, Jun. 2010, doi:10.1109/TPS.2010.2043690.
[13] C. D. Joye, J. P. Calame, A. M. Cook, and M. Garven, "High-power copper gratings for a sheet-beam traveling-wave amplifier at G-band," *IEEE Trans. Electron Devices*, vol. 60, no. 1, pp. 506-509, Jan. 2013, doi: 10.1109/TED.2012.2226591.
[14] N. M. Ryskin, A. G. Rozhnev, A. V. Starodubov, A. A. Serdobintsev, A. M. Pavlov, A. I. Benedik, R. A. Torgashov, G. V. Torgashov, and N. I. Sinitsyn, "Planar microstrip slow-wave structure for low-voltage *V*-band traveling-wave tube with a sheet electron beam, " *IEEE Electron Device Lett.*, vol. 39, no. 5, pp. 757-760, May 2018, doi: 10.1109/LED.2018.2821770.
[15] S. Fang, J. Xu, H. Yin, et al., "Experimental verification of the low transmission loss of a flat-roofed sine waveguide slow-wave structure, " *IEEE Electron Device Lett.*, vol. 40, no. 5, pp. 808-811, May 2019, doi: 10.1109/LED.2019.2904080.
[16] Y. M. Shin, A. Baig, L. R. Barnett, W. C. Tsai, and N. C. Luhmann, Jr., "System design analysis of a 0.22-THz sheet-beam traveling-wave tube amplifier," *IEEE Trans. Electron Devices*, vol. 59, no. 1, pp. 234-240, Jan. 2012, doi: 10.1109/TED.2011.2173575.
[17] Q. J. Lai, Y. B. Gong, X. Xu, Y. Y. Wei, et al., "W-band 1-kW staggered double-vane traveling-wave tube," *IEEE Trans. Electron Devices*, vol. 59, no. 2, pp. 496-503, Feb. 2012, doi: 10.1109/TED.2011.2174458.
[18] J. X. Wang, G. Liu, G. X. Shu, L. Yang, and Y. Luo, "Design and microwave measurement of a broadband compact power coupler for sheet beam traveling wave tubes," *IEEE Trans. Electron Devices*, vol. 63, no. 2, pp. 814-818, Feb. 2016, doi: 10.1109/TED.2015.2508480.
[19] G. X. Shu, J. Wang, G. Liu, L. Yang, Y. Luo, and S. F. Wang, "Design and microwave test of an ultra-wideband input/output structure for sheet beam travelling wave tubes, " *Review of Scientific Instrument*, vol. 86, no. 6, pp. 064703-1-064703-7, Jun. 2015, doi:10.1063/1.4922015.
[20] G. X. Shu, H. Xiong, L. H. Cao, H. X. Luo, G. Liu , J. X. Wang, Z. F. Qian, and W. L. He, "Design and millimeter-wave measurement of a wideband power coupling structure for sheet electron beam devices," *IEEE Trans. Electron Devices*, vol. 66, no. 7, pp. 3171-3177, Jun. 2019, doi: 10.1109/TED.2019.2916827.
[21] L. Y. Yang, J. X. Wang, G. X. Shu, G. Liu, E. A. Balfour, Y. L. Yao, K. Dong, H. Fu, and Y. Luo, "Design and measurement of a nonlinear-curve directional coupler for sheet beam traveling wave tube," *IEEE Transactions on Electron Devices*, vol. 63, no. 9, pp. 3733-3739, Sep. 2016, doi: 10.1109/TED.2016.2593663.
[22] G. X. Shu, J. X. Wang, G. Liu, Y. Luo, S. F. Wang, "An improved slow-wave structure for the sheet-beam traveling-wave tube," *IEEE Trans. Electron Devices*, vol. 63, no. 5, pp. 2089-2096, May 2016, doi: 10.1109/TED.2016.2535911.
[23] G. X. Shu, J. X. Wang, G. Liu, and Z. F. Qian, "Study of performance improvement for a Q-band sheet beam traveling-wave tube," *IEEE Transactions Electron Devices*, vol. 65, no. 9, pp. 3970-3975, May 2018, doi: 10.1109/TED.2018.2857920.
[24] R. Li , C. Ruan, S. Li, and H. F. Zhang, "G-band rectangular beam extended interaction klystron based on bi-periodic structure," IEEE Trans. Terahertz Sci. Technol., vol. 9, no. 5, pp. 498-504, Sep. 2019, doi: 10.1109/TTHZ.2019.2927857.
[25] D. Gamzina, L. G. Himes, R. Barchfeld, Y. Zheng, B. K. Popovic, C. Paoloni, E. Choi, and N. C. Luhmann, "Nano-CNC machining of sub-THz vacuum electron devices," *IEEE Trans. Electron Devices*, vol. 63, no. 10, pp. 4067-4073, Oct. 2016, doi: 10.1109/TED.2016. 2594027.
[26] A. Baig, Y. Shin, L. R. Barnett, D. Gamzina, R. Barchfeld, C. W. Domier, J. Wang, and N. C. Luhmann, Jr., "Design, fabrication and RF testing of near-THz sheet beam TWTA," *Terahertz Science Technology*, vol. 4, no. 4, pp. 181-207, Dec. 2011, doi: 10.11906/ TST.181-207. 2011.12.24.
[27] G. X. Shu, H. Yin, L. Zhang, J. Zhao, G. Liu, A. D. R. Phelps, A. W. Cross, and W. He, "Demonstration of a planar W-band, kW-level extended interaction oscillator based on a pseudospark-sourced sheet electron beam," *IEEE. Electron. Device. Lett.* vol. 39, no. 3, pp. 432-435, Apr. 2018, doi: 10.1109/LED.2018.2794469.
[28] A. M. Cook, C. D. Joye, R. L. Jaynes, and J. P. Calame, "W-band TWT circuit fabricated by 3D-printed mold electroforming," *in Proc. IEEE Int. Vac. Electron. Conf.*, Apr. 2018, pp. 331-332, doi: 10.1109/IVEC.2018.8391511.
[29] CST-Computer Simulation Technology. [Online]. Available: http://www.cst.com/products/cstmws, accessed Jun. 2019.
[30] M. P. Kirley and J. H. Booske, "Terahertz conductivity of copper surfaces," *IEEE Trans. THz Sci. Technol.*, vol. 5, no. 6, pp. 1012-1020, Nov. 2015, doi: 10.1109/TTHZ.2015.2468074.
[31] D. M. H. Hung, I. M. Rittersdorf, P. Zhang, et al. "Absolute Instability near the Band Edge of Traveling-Wave Amplifiers," Physical Review Letters, vol. 115, no. 12, pp. 124801-1-124801-5, 2015, doi: 10.1103/PhysRevLett.115.124801.
[32] A. S. Gilmour, Jr., Principles of Traveling-Wave Tubes. Boston, MA: Artech House, 1994.